



Embedded inkjet printed silver grids for ITO-free organic solar cells with high fill factor

Ignasi Burgués-Ceballos^{a,b}, Nikolaos Kehagias^c, Clivia M. Sotomayor-Torres^{c,d},
Mariano Campoy-Quiles^a, Paul D. Lacharmoise^{b,*}

^a Institut de Ciència de Materials de Barcelona (ICMAB-CSIC), Campus de la UAB, 08193 Bellaterra, Spain

^b Cetemmsa Technological Centre, Av. Ernest Lluch 36, 08302 Mataró, Spain

^c Institut Català de Nanociència i Nanotecnologia (ICN2), Campus de la UAB, 08193 Bellaterra (Barcelona), Spain

^d Institució Catalana de Recerca i Estudis Avançats (ICREA), 08010 Barcelona, Spain

ARTICLE INFO

Article history:

Received 3 February 2014

Received in revised form

11 March 2014

Accepted 13 March 2014

Available online 4 May 2014

Keywords:

ITO replacement

Silver grids

Embedded electrodes

Polymer solar cells

Reverse nanoimprinting transfer

Inkjet printing

ABSTRACT

We combine inkjet printed silver grids and reverse nanoimprinting transfer to demonstrate front electrode structures embedded within the substrate for indium tin oxide (ITO) replacement in organic solar cells. The smooth interface between Ag grid and transparent semiconductor polymer PEDOT:PSS improves the topology of the successive layers. In turn, this results in overall good photovoltaic performance including high fill factor and no shunting. By modelling the shadowing and resistive losses as a function of the separation between grid lines, the optimal grid structure is identified, which we then confirm experimentally. Inkjet printed ITO-free solar cells showed slightly higher performance than the ITO based reference.

© 2014 Elsevier B.V. All rights reserved.

1. Introduction

Indium tin oxide (ITO) has been widely used as a transparent electrode in rigid organic photovoltaic (OPV) devices due to its excellent properties [1,2], mainly its high stability and good compromise between transparency (~90%) and conductivity (sheet resistance of 8–12 Ω/sq) [3]. On the way to obtaining highly efficient, low-cost OPVs, the use of ITO has been identified as one of the main bottlenecks [4,5]. Additionally, the use of ITO in large flexible devices may not be recommended due to possible cracking or delamination and conductivity losses with bending [6].

Therefore, finding alternative transparent conductors is a major necessity. Many efforts are currently being carried out in this field. The goal is to find a cost-effective material with high conductivity, transparency and flexibility. Several ITO alternatives have been employed in OPV devices as transparent conductors. Alternatives include (i) transparent semiconductor polymer, namely poly(3,4-ethylenedioxythiophene), doped with poly(styrenesulfonate) (PEDOT:PSS) [7,8] or deposited from vapour phase [9], (ii) metal nanowires (NWs) [10,11] and ultrathin metal layers [12–14], (iii) combination of polymer and metal structures, typically in the form of grids covered by a PEDOT:PSS

layer [15,16] and (iv) carbon nanotubes (CNTs) [17,18] and graphene [19,20] films. Comprehensive reviews of works in this field can be found elsewhere [21–23]. However, more data and experimental work is still needed to determine whether a unique alternative or a combination of some of them will be predominant in the near future. A non-exhaustive selection of representative results obtained with these different electrode alternatives is shown in Table 1.

In all cases an inverse correlation between conductivity and transparency is observed. Thus, an optimum compromise is required to reach the highest OPV performance. PEDOT:PSS, [8] as well as its combination with metal NWs [10] and CNTs [18] are at this moment the materials performing most closely to ITO in terms of efficiency. However, when each structure is compared to its relative ITO reference ($\eta_{\text{ITO-free}}/\eta_{\text{ITO}}$ column) an interesting observation emerges: the combination of metal and PEDOT:PSS is a very successful ITO replacement, even doubling efficiency for large active areas. So far, metal grids have led to the largest OPV cell area with still reasonably good performances. Not surprisingly, they show the lowest sheet resistance (1 Ω/sq), which indicates that conductivity becomes a crucial factor for large area OPV applications [24]. Therefore, metal grids may be a good choice for large-scale OPVs when very high flexibility is not required. It is indicative that the first built OPV-based solar park uses such structures in both electrodes [25]. Major advantages such as significant reduction of material consumption and the possibility of recycling the metallic grid at the end of the

* Corresponding author. Tel.: +34 93 741 91 00; fax: +34 93 741 92 28.

E-mail address: placharmoise@cetemmsa.com (P.D. Lacharmoise).

Table 1

Alternatives to ITO. Representative electrodes and performance results in OPV devices. ρ : sheet resistance; T : transmittance; V_{oc} : open circuit voltage; J_{sc} : short circuit current density; FF: fill factor; PCE: power conversion efficiency; and $\eta_{ITO-free}/\eta_{ITO}$: PCE ratio.

Material		ρ (Ω/sq)	T (%)	Flexibility ^a	Active area (cm^2)	V_{oc} (V)	J_{sc} (mA cm^{-2})	FF (%)	PCE (%)	$\eta_{ITO-free}/\eta_{ITO}$	Reference
Metal oxide	ITO ^b	8–12	84	Low	0.15	0.63	9.5	68	0.95–5	–	[2–23]
Polymer	PEDOT:PSS	67	80	High	0.09	0.59	9.29	65	3.56	0.86	[11]
Metal	Metal NWs	12	85	High	0.07	0.42	2.8	25	0.3	0.07	[13]
	Ultrathin metal layers	NA	~50	Medium	0.09	0.58	7.12	61	2.52	0.72	[16]
		5	~30	Medium	35.5	6.8	5.8	40.3	0.44	NA	[17]
Metal + PEDOT:PSS	Metal NWs	12	85	High	0.07	0.62	10.4	65	4.2	1	[12]
	Metal grid	1	~70	Medium	4	0.54	6.25	57.1	1.93	2.03	[18]
		1	75	Medium	121.5	4.76	5.45	55.6	1.05	NA	[19]
Others	CNTs	60	~70	High	0.1	0.58	11.5	48	3.1	0.86	[21]
	Graphene	610	87	High	NA	0.60	9.03	48	2.6	0.68	[23]

^a Qualitative comparison of the flexibility of the material itself, taking into account the results presented in all references.

^b Sheet resistance and transparency values shown here are taken from Reference [3].

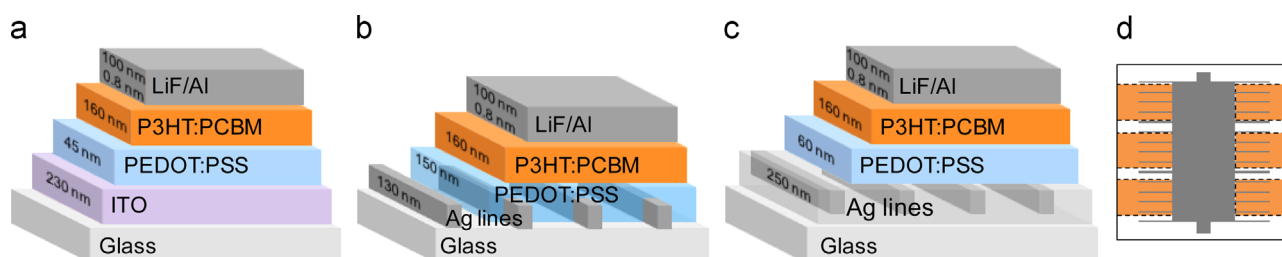


Fig. 1. Schematic cross sectional view of OPV devices (not to scale) with (a) ITO and with (b and c) silver grid lines as the front contact. Grids deposited on top of the substrate, i.e. originally protruding from the substrate surface, (b) may cause short circuits or current leakage or require a thick absorbing PEDOT:PSS layer. A solution to overcome this problem may be to embed the grids within the substrate (c). (d) Schematic front view of the inkjet printed Ag grid structures used in this study, comprising 6 OPV devices (coloured areas). (For interpretation of the references to colour in this figure legend, the reader is referred to the web version of this article.)

module lifetime [26], strongly motivate further research in these type of electrodes.

Metal grids must always be accompanied by a layer of a transparent conducting material such as PEDOT:PSS in order to allow transport of photogenerated charges towards the current collecting grid electrode. Different approaches for grid deposition have been successfully demonstrated in OPVs, including screen printing [15], inkjet printing [28], lithography [29] and thermal evaporation [30]. Even semi-transparent organic solar cells have been reported using metallic grids as both anode and cathode [31]. In order to get both high conductivity and transmittance with such structures, a compromise should be found between resistive losses and shadowing losses. The resistance of the Ag grid/PEDOT:PSS electrode should be kept as low as possible while at the same time the Ag grid surface coverage should be as small as possible to enable maximum solar light incidence in the active layer. Multiple grid configurations can be designed depending on several parameters, namely the sheet resistance of the PEDOT:PSS layer and both the bulk resistance and the 3D geometry of the Ag lines. A typical problem in such architectures lies in the difficulty to over-coat homogeneously these grid lines with thin layers of PEDOT:PSS and active layer, which leads to short circuits or current leakage in the best case. One solution is to deposit the PEDOT:PSS layer by rotary screen printing and in registry to the metallic grid structure [32]. An alternative solution may be to embed these grids within the substrate [15,33], which may allow to start PEDOT:PSS deposition on a flattened surface. Cross sectional views of 3 OPV device architectures are shown in Fig. 1.

In this work we show how embedding Ag grids in the substrate can lead to a significant improvement in OPV performance. Firstly, estimation of losses and fine tuning of the inkjet printing process lead to optimised grid geometry. Secondly, an easy, low-cost and potentially roll to roll (R2R) compatible reverse transfer technique is used to perform the embedding of the metallic structure. The flattened anode enables a more effective coating of the successive

layers. Finally, OPV devices with different anode structures are built and compared. In this work we differentiate between covered-only Ag grid structures (by PEDOT:PSS layer, Fig. 1b) and embedded structures (within the substrate, Fig. 1c).

2. Materials and methods

2.1. Inkjet printing of Ag lines

A Fujifilm Dimatix DMP-2800 piezoelectric drop-on-demand system was used to print the current collecting lines. The silver nanoparticle-based ink (SunTronic EMD 5603 from Sunchemical) was stirred and subsequently 0.45 μm PTFE and 0.20 μm PTFE filtered prior to loading into a 10 μL jet cartridge. The printing process was performed under ambient conditions at room temperature (for both the plate and the cartridge). For the embedded electrodes, Ag lines of 250 nm height and 100 μm width were printed onto the pre-cleaned glass substrates using two jets at a drop space of 40 μm . In contrast, for the covered-only electrodes, thinner lines (130 nm) were achieved by performing a 10 min O_2 plasma treatment on the glass substrates prior to printing with only 1 jet and an increased drop spacing of 50 μm . The piezoelectric firing voltage was set at 29 V in all cases, resulting in an ejection speed of ~ 13 m/s. Immediately after the printing process, the current collecting grids were annealed at 150 $^\circ\text{C}$ on a hot plate for 20 min in ambient conditions. The same processing conditions were used to inkjet print the complete series of Ag grid structures. The thickness and cross section areas of the printed Ag lines were measured with a Veeco Dektak 150 Profilometer. UV–vis spectrophotometry was carried out using a Varian Cary 5000 UV–vis–NIR spectrophotometer in transmission mode. A 25 mm^2 mask (equivalent to the active area of the OPV devices) was employed for the measurement.

2.2. Reverse nanoimprinting transfer

The 250 nm thick Ag grids were embedded within the substrate by reverse nanoimprinting transfer as follows (see Fig. 2): $2.5 \times 2.5 \text{ cm}^2$ glass substrates were cleaned by O_2 plasma at 400 W for 30 s. The samples were coated with Ormoprime08 (from Microresist Technology GmbH) to increase the surface adhesion of the printable resin (Ormocomp). Without this adhesion layer an unacceptable large number of grid transfer errors was observed. A drop of Ormocomp was dispensed on the pre-patterned glass substrates which contained the metal grid structures. The two substrates were then brought into contact while a pressure of 2 bars was applied for 1 min. The assembly was exposed to ultraviolet light for 10 s. After separation of the two substrates the Ag grid structures were embedded within the Ormocomp material and transferred to the pre-treated glass substrate.

In the present article rigid glass sacrificial substrates were used to print the grids as well as for the subsequent embedding. Moreover, the whole process could be transferred to flexible and continuous substrates. Ongoing work in this direction is being carried out.

2.3. Device fabrication

Patterned ITO-coated glass (purchased from Psiotec, Ltd.) and only-glass substrates (for the grid devices) were cleaned with soap water and successively ultrasonicated in acetone (15 min) and isopropanol (15 min). After nitrogen drying, the anode (or substrate, exclusively for the covered-only grid structure) was treated in an O_2 -plasma for 10 min. For the ITO-free devices no extra cleaning steps were performed after inkjet printing the Ag grids. On top of the anode, a 1 h degassed PEDOT:PSS ink (IJ1005 from Agfa-Orgacon) was doctor-bladed with a ZUA 2000 universal applicator (from Zehntner) at plate temperature of 50°C , a gap of $400 \mu\text{m}$ and a liquid volume of $50 \mu\text{L}$. The blade speed was set to 5 mm/s for ITO-based and for ITO-free devices. The speed was increased up to 10 mm/s for the ITO-free without embedded anode in order to obtain a thicker layer to cover the Ag lines fully (see Fig. 1). The resulting layer was then thermally annealed for 15 min at 90°C in a fume cabinet, resulting in layers of 45 nm, 60 nm and 150 nm in thickness for ITO-based, ITO-free embedded and ITO-free covered-only devices, respectively. Attempts to

reduce the PEDOT:PSS layer further for the ITO-free only covered devices with the aim of minimizing transparency losses resulted in frequent shortcut devices. Then, the organic layer was inkjet printed using the same Fujifilm Dimatix DMP-2800 printer as for the Ag grids, from a 1:1 poly(3-hexylthiophene)(P3HT):[6,6]-phenyl C_{61} -butyric acid methyl ester (PCBM) weight ratio solution (25 mg/mL in an o-dichlorobenzene/mesitylene mixture, 68:32) which had been stirred for 5 h at 60°C and filtered by a $0.2 \mu\text{m}$ nylon sieve prior to loading into a liquid crystal cartridge. The drop spacing was set to $30 \mu\text{m}$ and the substrate plate was kept at 40°C during printing. The inkjet head temperature was kept between 50 and 60°C and a typical firing voltage of 25 V was used, resulting in an ejection speed of $\sim 6 \text{ m/s}$. 96% regioregular-P3HT (Rieke Metals), PCBM (Solenne), o-DCB (Aldrich) and mesitylene (Aldrich) were used as delivered. The thickness of the organic layer was ca. 160 nm. The samples were then transferred to a nitrogen-filled glovebox and thermally annealed at 140°C for 10 min. The top cathode was deposited by sequential thermal evaporation of LiF (0.8 nm at a rate of 0.1 \AA/s) and Al (100 nm at $0.5\text{--}1 \text{ \AA/s}$) at $1 \times 10^{-6} \text{ mbar}$ through a shadow mask, defining an active area of 25 mm^2 .

The current–voltage characteristics of the solar cells were measured under AM 1.5 G (Air Mass 1.5 Global) illumination, 100 mW/cm^2 , with an Atlas SolarTest 1200 solar simulator and a Keithley 2602A SourceMeter under ambient conditions.

3. Calculations of losses

To estimate shadowing and resistive losses of the Ag grid/PEDOT:PSS electrode, a numerical model described in the literature [34] was adapted to this specific material system and modified to include the linear geometry, i.e., parallel lines, of the silver grid. Using the typical parameters for the materials used, we found no evidence that other geometries, such as honeycomb structure, would result in a more efficient current collection. Moreover, another reason to keep a linear geometry is that the narrowest lines accessible by inkjet printing are those parallel to the displacement of the print head, a condition not feasible for a honeycomb structure. Therefore, as minimum shadowing losses are mandatory for this application, we concluded that the linear geometry may be the best design for this particular printing

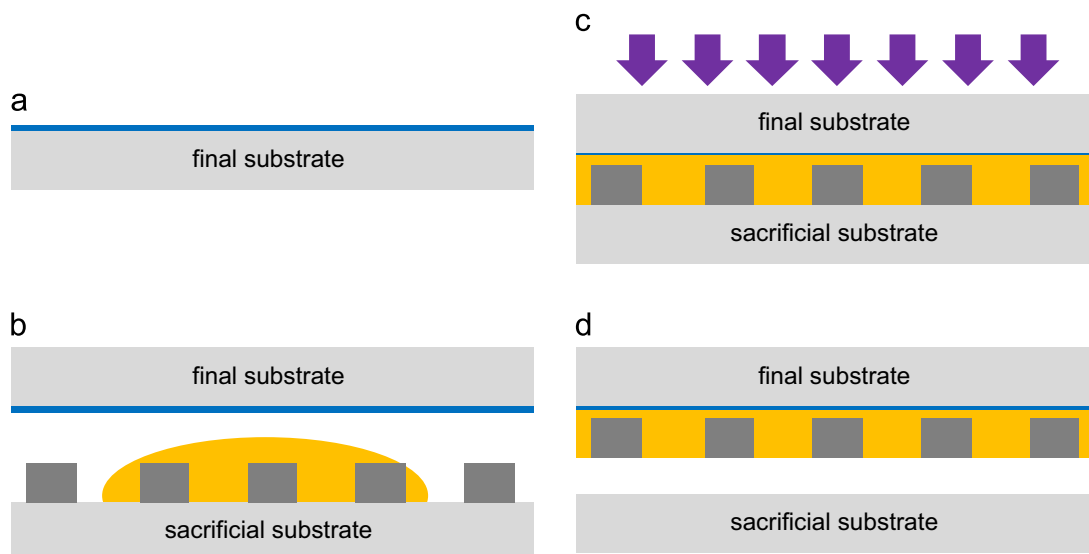


Fig. 2. Reverse nanoimprinting transfer to embed Ag grids. (a) An adhesion promoter (Ormoprime08) is coated on a pre-treated (final) substrate. (b) A UV curing resin is drop casted onto the sacrificial glass/Ag grid structure. (c) The two substrates are assembled and pressure and UV light exposure are applied subsequently and (d) Finally, the two substrates are separated leading to the desired embedded Ag grid structure.

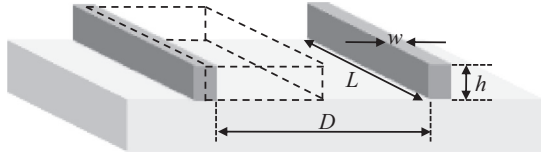


Fig. 3. Scheme of the unit cell (dashed lines) and the dimensional parameters. Length (L), width (w) and height (h) of the Ag line are fixed in the calculations whereas the distance between lines, i.e., pitch (D), is varied. The sheet resistance of PEDOT:PSS (ρ_{sh}) and the bulk resistivity of inkjet printed Ag (ρ_M) are also input values in the calculation. Note that the scheme is not at scale; w is in the μm range while h is in the nm range.

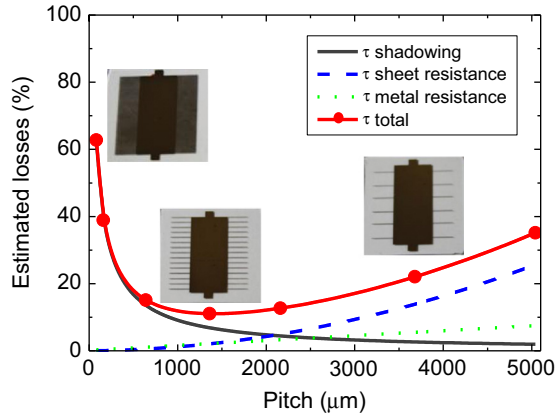


Fig. 4. Estimated losses in current collection as a function of separation between lines. The circles overlapped with the total losses curve correspond to the series of samples with embedded grids that were prepared in this work. The inset photographs were taken from three representative samples with expected high shadowing (left), optimised geometry (middle) and high resistive losses (right). The central opaque part is the collection pad (see Fig. 1d).

technique. Fig. 3 shows the unit cell and the parameters involved in the calculation of losses.

The input parameters involved in these calculations are experimentally measured: the sheet resistance of PEDOT:PSS ($\rho_{sh} \sim 800 \Omega/\text{sq}$), the bulk resistivity of inkjet printed Ag ($\rho_M \sim 3 \cdot 10^{-7} \Omega \text{ m}$), and the height (h , 130 or 250 nm), width ($w = 100 \mu\text{m}$) and length ($L = 5 \text{ mm}$, fixed in the printing pattern) of the Ag lines. The only parameter we varied was the pitch (D). A typical OPV performance has to also be taken into account. A voltage (V_{mpp}) and current density (J_{mpp}) at the maximum power point of 0.48 V and of 7 mA cm^{-2} , respectively, were considered taking as a reference the 3.5% efficient organic solar cell presented by Hoth et al. with inkjet printed active layer [35], since the solar cells in this work were fabricated in a similar manner. Further calculations made with the results obtained in the present study (see Section 4) revealed negligible changes in the optimal pitch.

As a result, the individual contributions to losses in current collection are [34]

Losses from shadowing

$$\tau_{\text{shadow}} = \frac{w}{w+D}$$

Losses from sheet resistance of the PEDOT:PSS layer

$$\tau_{\text{sheet R}} = \frac{J_{mpp}}{V_{mpp}} \frac{(w+D)^2}{12} \rho_{sh}$$

Losses from metal resistance of the Ag lines

$$\tau_{\text{metal R}} = \frac{J_{mpp}}{3 V_{mpp}} \frac{(w+D)L^2}{h w} \rho_M$$

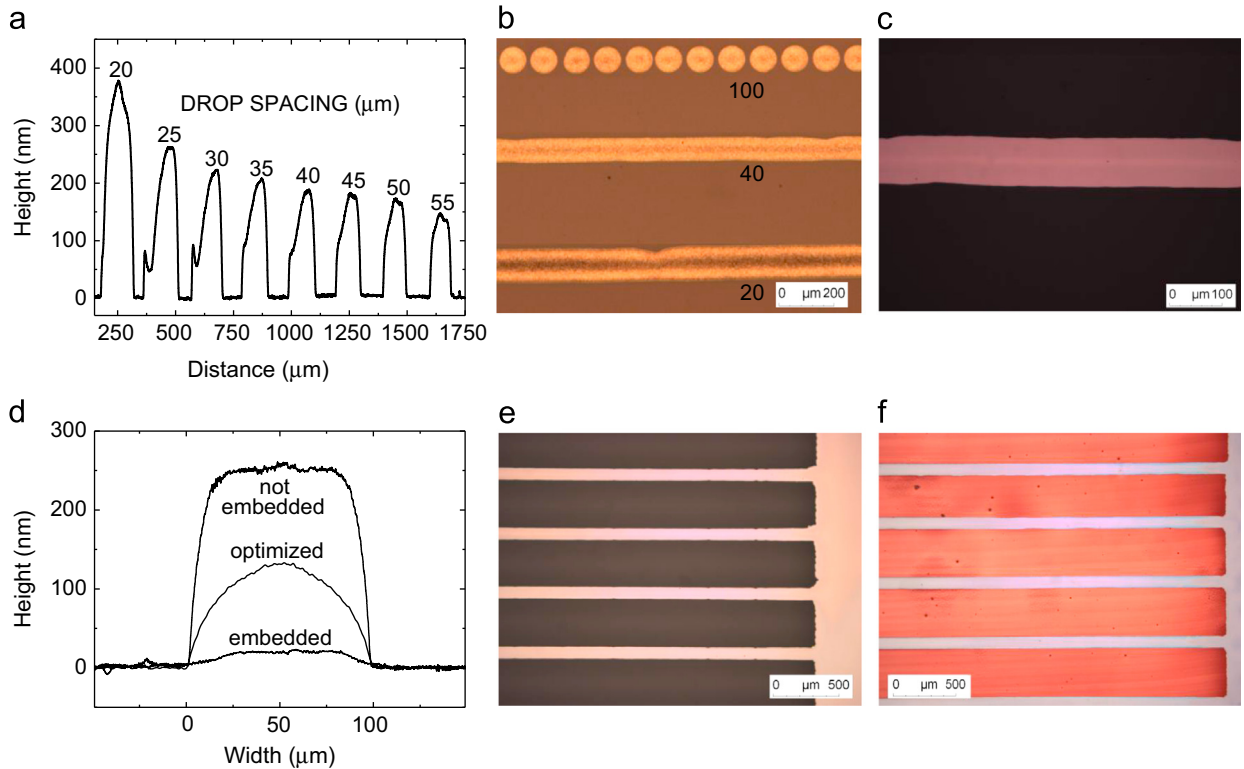


Fig. 5. Optimisation of inkjet printing process: (a) cross section profiles and (b) micrograph of silver lines printed at different drop spacing. This test is performed to find the conditions that lead to (c) narrow, continuous and coffee ring-free lines. (d) An optimised process enabled the reduction of the line height from 250 nm (upper trace) to 130 nm (middle trace), while its width remained constant at $100 \mu\text{m}$. After embedding the non-optimised line, only 20 nm of Ag protruded from the surface (bottom trace). Inkjet printed Ag grid (b) before and (c) after the fabrication of the solar cell device (bottom view).

Losses from interface contact between Ag lines and PEDOT:PSS were not considered in this work, as they might be negligible in comparison to the sheet resistance of PEDOT:PSS.

Fig. 4 shows the estimated losses against the pitch, where it is clearly visible how shadowing governs in the regime with small separation between lines and the resistive losses become dominant at larger pitch, mostly because of the sheet resistance of PEDOT:PSS. This tendency is in accordance to other works that employed a similar modelling approach [36]. The full circles in Fig. 4 correspond to the selection of grid patterns printed in this work and subsequently embedded.

4. Results and discussion

4.1. Inkjet printing of current-collecting Ag lines

The desired geometry of a current-collecting grid has to accomplish an optimal balance between transparency and conductivity. The former can be achieved by reducing the line width as much as possible as well as by increasing the pitch. On the other hand, a higher conductivity is obtained with higher line density, that is, with a smaller pitch. Alternatively, the conductivity can be increased by increasing the metal lines thickness, as described elsewhere [29]. However, overly thick lines may cause current leakage and shorts unless they are embedded within the substrate, as explained in the first section.

Although lithographic mould-based metal grids can lead to narrower lines [29], inkjet printing may be an interesting, lower cost technique due to its compatibility with R2R processes and its mask-less nature. Some examples of inkjet printed current-collecting grids have been presented in the field of OPVs [28,37]. In all cases a thick PEDOT:PSS layer was deposited on the grids to cover them entirely, ideally with a thicker layer than the printed

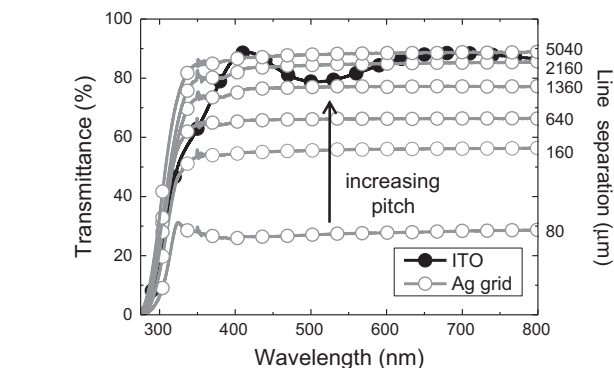









Fig. 6. Transmittance through embedded Ag grids with different line separation compared to ITO on glass. A 25 mm² mask (equivalent to the active area of the OPV devices) was employed for the measurement.

Table 2
Properties of the series of substrates with embedded Ag grids.

Pitch (μm)	80	160	640	1360	2160	3680	5040	Glass
Surface coverage (%)	62.5	38.5	13.5	6.8	4.4	2.6	1.9	0
Estimated total losses (%)	62.8	38.9	15.1	11.1	12.7	22.0	35.1	100
Transmittance at 550 nm (%)	27.5	55.9	66.3	77.1	84.7	87.9	88.2	90.5
Picture								

line height [38] with the consequence of a significant loss in transparency.

In order to assess the effect of embedding the grids, two different configurations of Ag lines were tested. First, as the height of the line is not the limiting factor for the embedded electrodes, 250 nm thick grid lines were inkjet printed (see Fig. 5). This ensures high conductivity. The minimum line width achieved was 100 μm. Second, for the covered-only electrodes, thinner lines were intended to avoid current leakage in the OPV devices. For this purpose, an O₂ plasma treatment was performed on the glass substrates, which significantly enhanced the wettability of the Ag ink. The latter allowed for both an increase in the drop spacing and the use of only 1 jet for printing continuous lines (see Section 2). As a result, the height of the Ag lines was reduced to 130 nm maintaining the 100 μm width, as shown in Fig. 5d. To the best of our knowledge, these are the thinnest metallic structures obtained by inkjet printing so far.

4.2. Reverse nanoimprinting transfer

The 250 nm thick Ag grids were embedded within the substrate by a simple, cost-effective method which is, additionally, potentially compatible with roll-to-roll processing. After the embedding step, only 20 nm of the original 250 nm of Ag lines protruded from the surface (Fig. 5d), which equals 92% of embedding. This approach offers significant advantages. First, it enables the Ag grid to be overcoated with an optimal film thickness of PEDOT:PSS layer (Fig. 1c). Moreover, the smoothening of the surface facilitates a much more homogenous active layer deposition (Fig. 5f). Both this homogeneity and the lowering of current leakage are responsible for the improvement in fill factor observed in the *J*–*V* curves, as we will show in the following section.

Concerning transparency, Fig. 6 shows the transmittance of these structures for various pitches. As the separation between lines increases, a higher transmittance is obtained. The expected optimal region shows transmittances of around 80%, equivalent to the glass/ITO structure, with the advantage of showing a more flattened response in the visible region.

All these relevant parameters are summarized in Table 2 for the series of selected points from Fig. 4. Note that the estimated pitches are multiples of 80 μm. This is exactly twice the drop spacing used for this series of Ag grids, as they were inkjet printed with two jets.

4.3. OPV with embedded Ag grids

In a similar way as in the work of Galagan et al. [39], the influence of the pitch in the OPV performance was studied. In our case, only the series of embedded Ag grids were considered. When the photovoltaic characteristics of these selected devices are plotted as a function of the separation between lines, a high correlation with the estimated losses is observed (Fig. 7). The

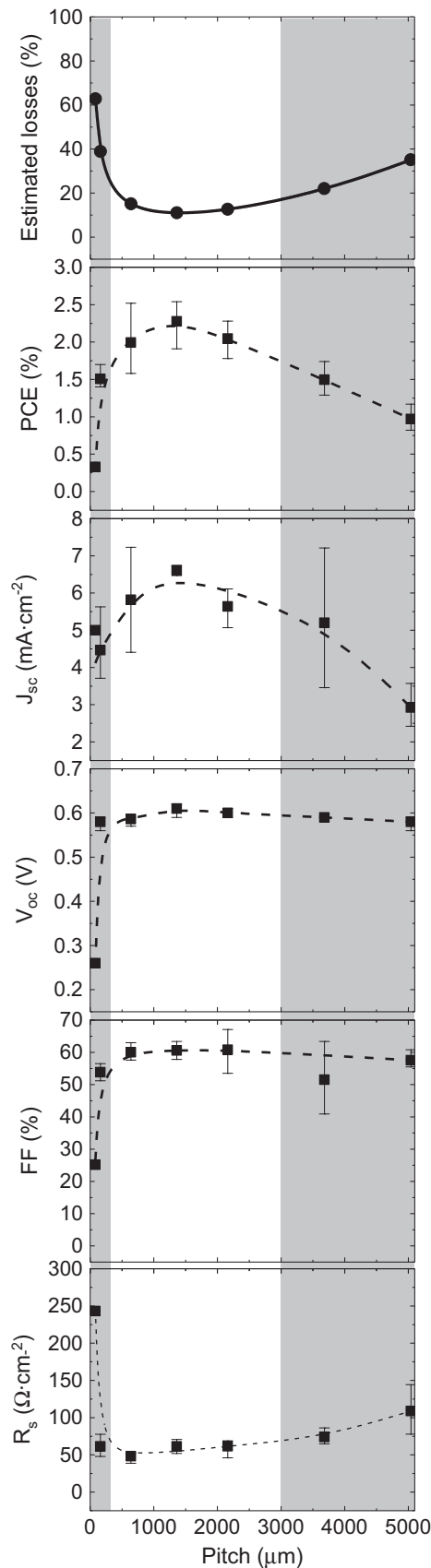


Fig. 7. Dependence of OPV performance parameters on the pitch compared to predicted losses. Greyed areas indicate the regimes where shadowing (left) too high and resistive losses (right) limit the current extraction.

dependence of PCE on the pitch is a curve with exceptionally high mirror symmetry with the curve of estimated losses. These results demonstrate that there is a good correlation between predictions and experimental results, thus the adapted model for estimating losses of Ag grids appears to be validated.

Further examination of Fig. 7 shows how the current generation J_{sc} is limited by the shadowing effect for small pitch. A maximum is reached at medium pitches, and then J_{sc} diminishes again at a slower rate at a larger pitch where charge extraction is reduced by resistive losses. On the other hand, V_{oc} and FF show similar trends: (a) low values are obtained at high density of grid lines due to poor rectification, presumably derived from inadequate morphology and/or higher current leakage; and (b) the crowding of lines increases the probability of microshunts, probably due to an eventual, faulty embedding. Then, a maximum is rapidly reached followed by a plateau from there on. Finally, the series resistance (R_s) follows a similar tendency as the estimated losses. This is in good agreement with the work of Tvingstedt et al. where they conclude that the cell series resistance becomes large when the Ag grid is too closely or too widely spaced [36]. As discussed in Section 3, the resistive losses govern at large pitches (Fig. 4), mostly due to PEDOT:PSS. It is thus obvious that this layer is the main responsible for the increase in the series resistance. On the other hand, the origin of the high R_s with low line separation might be less intuitive. As suggested above, we ascribe this to a poorer coverage of the grid lines. Even with an embedded structure, a higher line concentration entails a higher risk of differences in line height or topography. This may lead to microshunts (lower parallel resistance) and/or poorer contact between metallic lines and PEDOT:PSS (higher series resistance). In this specific case, the contact resistance in this interface, which has been omitted in the estimation of losses, might not be negligible.

Organic solar cells with three designs depicted in Fig. 1 were fabricated with the optimised grid geometry. Besides the anode and the PEDOT:PSS layer thickness, the rest of the structure was constructed identically in order to enable comparison. The current density–voltage (J – V) characteristics of the optimised devices (Fig. 8) unquestionably show relevant improvement from covered-only to embedded Ag grid structures in all cell parameters (see also Table 3). The lower values of (mainly) the short-circuit current, fill factor and parallel resistance obtained with the covered-only anodes are evidence that current leakage is strong, as expected. The 52% of FF is likewise in the same order of similar devices described in the literature [28]. On the contrary, the J – V curve of the embedded structure shows a much better rectification: low series resistance,

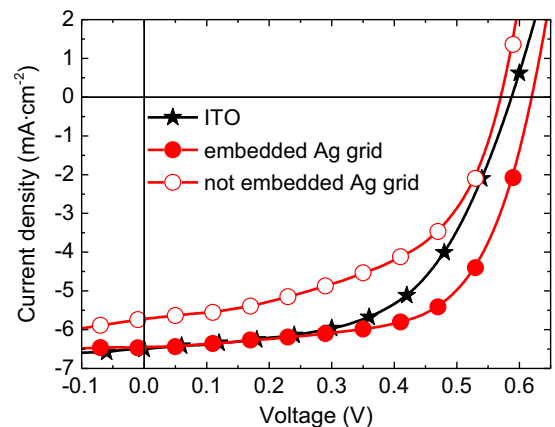


Fig. 8. J – V curves of optimised organic solar cells built on different anode structures.

Table 3
Photovoltaic characteristics of the organic solar cells based on different anodes.

Anode	V_{oc} (V)	J_{sc} (mA cm ^{−2})	FF (%)	PCE (%)	R_s (Ω cm ^{−2})	R_p (Ω cm ^{−2})
ITO	0.59	6.50	57	2.15	20.0	1734
Embedded Ag grid	0.62	6.46	63	2.54	11.5	3425
Not embedded Ag grid	0.57	5.71	52	1.70	14.2	463

high parallel resistance and high FF. This is a result of a flattened interface between Ag grid and PEDOT:PSS [33]. As far as we know, this is the highest reported value for FF in ITO-free devices containing Ag grids processed in air conditions, with the exception of the cathode deposition. The highest FF obtained in the studied series of devices was 67%. In turn, J_{sc} is almost the same as for the ITO-based device, which indicates that the grid structure has the same current collecting capability as ITO. However, the PCE values are lower than expected. It can be concluded that J_{sc} is the main cause of this, considering that good rectification and open circuit voltages (V_{oc}) are obtained. Consequently, other factors besides the anode may be behind this, such as active material degradation. Even so, the $\eta_{ITO-free}/\eta_{ITO}$ ratio for the embedded structure is higher than 1, which is also in accordance with results in Table 1.

5. Conclusions

We have shown the entire process of optimisation of current collecting Ag grids made by inkjet printing for ITO replacement in organic solar cells. First, we optimised the inkjet printing processing conditions to get the thinnest possible Ag lines (130 nm). Following this we demonstrated the reverse nanoimprinting transfer as an easy, low-cost and potentially R2R-compatible technique to embed Ag grid structures (embedding > 90%). Higher homogeneity in subsequent layers was achieved using this improved anode interface while the risk of current leakage was significantly reduced. This resulted in an enhancement in the fill factor (FF > 60%) of the solar cell device. This ITO-free structure has similar current collecting capability as ITO. Finally, the influence of the distance between grid lines was successfully correlated with the photovoltaic performance of the devices, thus validating the model used for the Ag grid optimisation.

Acknowledgements

This work was financially supported by the Spanish Ministerio de Economía y Competitividad through projects MAT2009-10642, MAT2012-37776 and Cetemmsa Technological Centre (Project no. CSIC-20091449). I.B.C wishes to thank the Universitat Autònoma de Barcelona (UAB) for the support given through the Chemistry Ph.D. programme.

References

[1] B.C.J. Brabec, N.S. Sariciftci, J.C. Hummelen, Plastic Solar Cells, *Adv. Funct. Mater.* (2001) 15–26.
 [2] W.L. Ma, C.Y. Yang, X. Gong, K. Lee, a J. Heeger, Thermally stable, efficient polymer solar cells with nanoscale control of the interpenetrating network morphology, *Adv. Funct. Mater.* 15 (2005) 1617–1622.
 [3] Sigma-Aldrich.
 [4] N. Espinosa, R. García-Valverde, A. Urbina, F.C. Krebs, A life cycle analysis of polymer solar cell modules prepared using roll-to-roll methods under ambient conditions, *Sol. Energy Mater. Sol. Cells* 95 (2011) 1293–1302.
 [5] B. Azzopardi, C.J.M. Emmott, A. Urbina, F.C. Krebs, J. Mutale, J. Nelson, Economic assessment of solar electricity production from organic-based

photovoltaic modules in a domestic environment, *Energy Environ. Sci.* 4 (2011) 3741.
 [6] D.R. Cairns, R.P. Witte II, D.K. Sparacin, S.M. Sachsman, D.C. Paine, G. P. Crawford, et al., Strain-dependent electrical resistance of tin-doped indium oxide on polymer substrates, *Appl. Phys. Lett.* 76 (2000) 1425.
 [7] T. Aernouts, P. Vanlaeke, W. Geens, J. Poortmans, P. Heremans, S. Borghs, et al., Printable anodes for flexible organic solar cell modules, *Thin Solid Films* 451–452 (2004) 22–25.
 [8] Y. Xia, K. Sun, J. Ouyang, Solution-processed metallic conducting polymer films as transparent electrode of optoelectronic devices, *Adv. Mater.* 24 (2012) 2436–2440.
 [9] X. Wang, T. Ishwara, W. Gong, M. Campoy-Quiles, J. Nelson, D.D.C. Bradley, High-performance metal-free solar cells using stamp transfer printed vapor phase polymerized poly(3,4-ethylenedioxythiophene) top anodes, *Adv. Funct. Mater.* 22 (2012) 1454–1460.
 [10] W. Gaynor, G.F. Burkhard, M.D. McGehee, P. Peumans, Smooth nanowire/polymer composite transparent electrodes, *Adv. Mater.* 23 (2011) 2905–2910.
 [11] J. Ajuria, I. Ugarte, W. Cambarau, I. Etxebarria, R. Tena-Zaera, R. Pacios, Insights on the working principles of flexible and efficient ITO-free organic solar cells based on solution processed Ag nanowire electrodes, *Sol. Energy Mater. Sol. Cells* 102 (2012) 148–152.
 [12] J. Meiss, M.K. Riede, K. Leo, Towards efficient tin-doped indium oxide (ITO)-free inverted organic solar cells using metal cathodes, *Appl. Phys. Lett.* 94 (2009) 013303.
 [13] J. Ajuria, I. Etxebarria, W. Cambarau, U. Muñecas, R. Tena-Zaera, J.C. Jimeno, et al., Inverted ITO-free organic solar cells based on p and n semiconducting oxides. New designs for integration in tandem cells, top or bottom detecting devices, and photovoltaic windows, *Energy Environ. Sci.* 4 (2011) 453.
 [14] D. Angmo, M. Hosel, F.C. Krebs, All solution processing of ITO-free organic solar cell modules directly on barrier foil, *Sol. Energy Mater. Sol. Cells* 107 (2012) 329–336.
 [15] Y. Galagan, J.-E.J.M. Rubingh, R. Andriessen, C.-C. Fan, P.W.M. Blom, S. C. Veenstra, et al., ITO-free flexible organic solar cells with printed current collecting grids, *Sol. Energy Mater. Sol. Cells* 95 (2011) 1339–1343.
 [16] D. Angmo, S.A. Gevorgyan, T.T. Larsen-Olsen, R. Søndergaard, M. Ho sel, M. Jørgensen, et al., Scalability and stability of very thin, roll-to-roll processed, large area, indium-tin-oxide free polymer solar cell modules, *Org. Electron.* 14 (2013) 984–994.
 [17] A. Du Pasquier, H.E. Unalan, A. Kanwal, S. Miller, M. Chhowalla, Conducting and transparent single-wall carbon nanotube electrodes for polymer-fullerene solar cells, *Appl. Phys. Lett.* 87 (2005) 203511.
 [18] R.C. Tenent, T.M. Barnes, J.D. Bergeson, A.J. Ferguson, B. To, L.M. Gedvilas, et al., Ultrasoother, large-area, high-uniformity, conductive transparent single-walled-carbon-nanotube films for photovoltaics produced by ultrasonic spraying, *Adv. Mater.* 21 (2009) 3210–3216.
 [19] J. Wu, H.A. Becerrii, Z. Bao, Z. Liu, Y. Chen, P. Peumans, Organic solar cells with solution-processed graphene transparent electrodes, *Appl. Phys. Lett.* 92 (2008) 263302.
 [20] M. Choe, B.H. Lee, G. Jo, J. Park, W. Park, S. Lee, et al., Efficient bulk-heterojunction photovoltaic cells with transparent multi-layer graphene electrodes, *Org. Electron.* 11 (2010) 1864–1869.
 [21] D. Angmo, F.C. Krebs, Flexible ITO-free polymer solar cells, *J. Appl. Polym. Sci.* 129 (2013) 1–14.
 [22] A. Kumar, C. Zhou, The race to replace tin-doped indium oxide: which material will win? *ACS Nano* 4 (2010) 11–14.
 [23] C.J.M. Emmott, A. Urbina, J. Nelson, Environmental and economic assessment of ITO-free electrodes for organic solar cells, *Sol. Energy Mater. Sol. Cells* 97 (2012) 14–21.
 [24] J.D. Servaites, S. Yeganeh, T.J. Marks, M.A. Ratner, Efficiency enhancement in organic photovoltaic cells: consequences of optimizing series resistance, *Adv. Funct. Mater.* 20 (2010) 97–104.
 [25] F.C. Krebs, N. Espinosa, M. Hosel, R.R. Søndergaard, M. Jørgensen, 25th anniversary article: rise to power – OPV-based solar parks, *Adv. Mater.* 26 (2014) 29–39.
 [26] T.T. Larsen-Olsen, R.R. Søndergaard, K. Norrman, M. Jørgensen, F.C. Krebs, All printed transparent electrodes through an electrical switching mechanism: a convincing alternative to indium-tin-oxide, silver and vacuum, *Energy Environ. Sci.* 5 (2012) 9467.
 [27] Y. Galagan, E.W.C. Coenen, S. Sabik, H.H. Gortler, M. Barink, S.C. Veenstra, et al., Evaluation of ink-jet printed current collecting grids and busbars for ITO-free organic solar cells, *Sol. Energy Mater. Sol. Cells* 104 (2012) 32–38.
 [28] M.-G. Kang, M.-S. Kim, J. Kim, L.J. Guo, Organic solar cells using nanoimprinted transparent metal electrodes, *Adv. Mater.* 20 (2008) 4408–4413.
 [29] M. Glatthaar, M. Niggemann, B. Zimmermann, P. Lewer, M. Riedea. Hinschet al., Organic solar cells using inverted layer sequence, *Thin Solid Films.* 491 (2005) 298–300.
 [30] T.R. Andersen, H.F. Dam, B. Andreasen, M. Hosel, M.V. Madsen, S.A. Gevorgyan, et al., A rational method for developing and testing stable flexible indium- and vacuum-free multilayer tandem polymer solar cells comprising up to twelve roll processed layers, *Sol. Energy Mater. Sol. Cells* 120 (2014) 735–743.
 [31] M. Hosel, R.R. Søndergaard, M. Jørgensen, F.C. Krebs, Fast inline roll-to-roll printing for indium-tin-oxide-free polymer solar cells using automatic registration, *Energy Technol.* 1 (2013) 102–107.
 [32] J.-S. Yu, I. Kim, J.-S. Kim, J. Jo, T.T. Larsen-Olsen, R.R. Søndergaard, et al., Silver front electrode grids for ITO-free all printed polymer solar cells with embedded and raised topographies, prepared by thermal imprint, flexographic and inkjet roll-to-roll processes, *Nanoscale* 4 (2012) 6032.

- [34] A. Cheknane, B. Benyoucef, J.-P. Charles, R. Zerdoum, M. Trari, Minimization of the effect of the collecting grid in a solar cell based silicon, *Sol. Energy Mater. Sol. Cells* 87 (2005) 557–565.
- [35] C.N. Hoth, P. Schilinsky, S.A. Choulis, C.J. Brabec, Printing highly efficient organic solar cells, *Nano Lett.* 8 (2008) 2806–2813.
- [36] K. Tvingstedt, O. Inganäs, Electrode grids for ITO free organic photovoltaic devices, *Adv. Mater.* 19 (2007) 2893–2897.
- [37] M. Neophytou, E. Georgiou, M.M. Fyrillas, S.A. Choulis, Two step sintering process and metal grid design optimization for highly efficient ITO free organic photovoltaics, *Sol. Energy Mater. Sol. Cells* 122 (2014) 1–7.
- [38] M. Neophytou, F. Hermerschmidt, A. Savva, E. Georgiou, S.A. Choulis, Highly efficient indium tin oxide-free organic photovoltaics using inkjet-printed silver nanoparticle current collecting grids, *Appl. Phys. Lett.* 101 (2012) 193302.
- [39] Y. Galagan, B. Zimmermann, E.W.C. Coenen, M. Jørgensen, D.M. Tanenbaum, F. C. Krebs, et al., Current collecting grids for ITO-free solar cells, *Adv. Energy Mater* 2 (2012) 103–110.